Int J Mater Form (2011) 4:129–140
DOI 10.1007/s12289-010-1013-8

THEMATIC ISSUE: TWENTE

Simulation of stretch forming with intermediate heat treatments of aircraft skins

A physically based modeling approach

Srihari Kurukuri · Alexis Miroux · Harm Wisselink · Ton van den Boogaard

Received: 11 May 2010 / Accepted: 29 November 2010 / Published online: 23 December 2010

Abstract In the aerospace industry stretch forming is often used to produce skin parts. During stretch forming a sheet is clamped at two sides and stretched over a die, such that the sheet gets the shape of the die. However for complex shapes it is necessary to use expensive intermediate heat-treatments in between, in order to avoid Lüders lines and still achieve large deformations. To optimize this process FEM simulations are performed. The accuracy of finite element analysis depends largely on the material models that describe the work hardening during stretching and residual stresses and work hardening reduction during heat treatments due to recovery and particle coarsening. In this paper, a physically based material modeling approach used to simulate the stretch forming with intermediate heat treatments and its predictive capabilities is verified. The work hardening effect during stretching is calculated using the dislocation density based Nes model and the particle coarsening and static recovery effects are modeled with simple expressions based on physical observations. For comparison the simulations are also performed with a phenomenological approach of work hardening using a power law. The Vegter yield function is used to account for the anisotropic and biaxial behavior of the aluminum sheet. A leading edge skin part, made of AA 2024 has been chosen for the study. The strains in the part have been measured and are used for validation of the simulations. From the used FEM model and the experimental results, satisfactory results are obtained for the simulation of stretching of aircraft skins with intermediate heat treatments and it is concluded that the physics based material modeling gives better results.

Keywords Stretch forming · Heat treatment · Material model · Aluminum sheet · FEM simulation

S. Kurukuri (✉) · A. Miroux · H. Wisselink
Materials Innovation Institute (M2i), P.O. Box 5008,
2600 GA Delft, The Netherlands
e-mail: s.kurukuri@m2i.nl, s.kurukuri@gmail.com

S. Kurukuri · H. Wisselink · T. van den Boogaard
Faculty of Engineering Technology, University of Twente,
P.O. Box 217, 7500 AE Enschede, The Netherlands

H. Wisselink
e-mail: h.wisselink@m2i.nl

T. van den Boogaard
e-mail: a.h.vandenboogaard@utwente.nl

A. Miroux
Faculty of 3mE, Delft University of Technology,
P.O. Box 5025, 2600 GA Delft, The Netherlands
e-mail: a.miroux@m2i.nl

Introduction

Stretch forming is a process in which a desired shape is obtained by stretching a sheet blank or extrusion sections over a tool surface while applying a tensile stress. It is a manufacturing process well suited to the fabrication of parts which are convex in nature, with relatively low levels of bending [1]. This often makes stretch forming the process of choice in the aircraft industry for manufacturing of large open shapes such as wing leading edges and engine cowlings [2]. The basic principles of the stretch forming process of the leading edge of an aircraft wing is shown in Fig. 1. An advantage of this process is that only one die is needed. The undeformed sheet is clamped with two

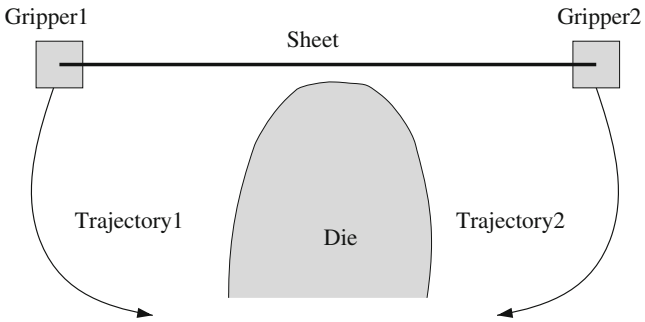

Fig. 1 Principle of stretch forming

CNC controllable grippers which determine the trajectory of deformation of the clamped sheet relative to the die.

The stretch forming of the leading edge can be divided into four steps. During the first step, the sheet is draped around the die without any contact with the die by moving the grippers towards each other. In the second step, the grippers are moved down until the sheet touches the die. During the third stage, the sheet is stretched plastically around the die until the sheet and die are completely in contact. In the last stretching step, extra strains are induced in the sheet by moving the grippers vertically downwards in order to minimize the effect of spring back [3].

The most commonly used material for aircraft skin parts is the heat treatable aluminum alloy AA 2024. In the fabrication of significant doubly curved surfaces using heat treatable aluminum alloy sheet, large strain gradients are induced across the part. That can lead to surface defects like Lüder lines and orange peel, causing rejection of the components. In order to avoid these failures and still achieve large deformations, a multi stage forming approach is normally employed. In this procedure several forming steps with intermediate annealing treatments are employed to return the sheet to a more ductile condition [2, 4].

Traditionally, the forming steps with inter-stage annealing and the die shape are defined using production experience and are improved by trial and error. This is a costly and time consuming way that may lead to sub-optimal solutions. Models of the stretch forming process are useful to achieve such an optimal process control. The advantage of models is that they can be used before the tools are made, avoiding lengthy and expensive trial and error runs for modifications of the tools and for reducing the number of expensive intermediate annealing steps. "Thorough" models, such as models based on the finite element method are needed to gain fundamental knowledge of the stretch forming process [5, 6]. Hence the goal of the finite element model is to facilitate the optimization of the number and possibly the duration of each intermediate annealing step and therefore of the whole process. However, material models used in the finite element analysis of stretch forming of aircraft skin parts with intermediate heat treatments are still mainly based on phenomenological laws [6]. Hence, further improvement requires the use of a set of thermo-mechanical material models that explicitly consider the effect of microstructure on plastic deformation, the static recovery and particle coarsening due to precipitation during intermediate heat treatment [7]. These physical mechanisms should be modeled up to a level that is required for macroscopic process simulations.

Stretch forming characterization tests for AA 2024

The stretch forming process used for producing the aircraft skin part consists of several deformation steps with intermediate annealing treatments at 340 °C. The annealing treatments reduce the strain hardening of the previous step. The material properties of AA 2024 are well known for several tempering conditions, amongst others the high strength conditions (T3, T4, T8 and their derivatives), and also the full-annealed condition [8]. However, the properties after intermediate annealing for AA 2024 are unknown. Only a schematic graph of the influence of several ageing and overageing conditions are given by [8]. This graph shows that the strength decreases due to overageing while the strain to fracture only increases upon strong overageing.

A number of tensile tests were performed at National Aerospace Laboratory (NLR) by Stork Fokker and NLR, in order to understand the effect of intermediate annealing steps on stretching. Tests were performed on AA 2024 Clad in T3 condition with a thickness of 1.6 mm. Each sample was first annealed at a temperature of 340 °C for different annealing times, which is a common treatment to relieve stress. After this treatment the samples were given several strain steps with each strain step followed by an intermediate heat treatment. All the samples considered were loaded in the rolling direction with the strains applied in one or two steps (2 %, 4 %, 6 %, and 2 × 2.5 %). Complete details of these experimental results were published in [2, 9]. These results are used for validating and comparing the implemented material models in this work. For brevity, the important findings are described here. In [2], it was found that, the first annealing treatment applied on T3 material causes a large decrease of the mechanical properties. The ultimate tensile strength decreases from 440 MPa to 290 MPa, yield strength drops from 340 MPa to 170 MPa and fracture strain

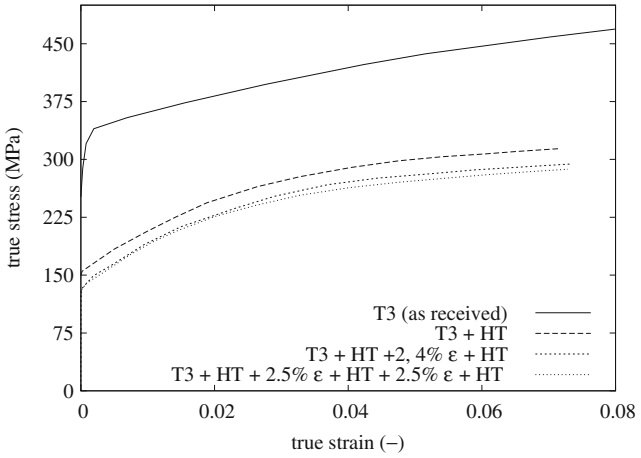

Fig. 2 Experimental stress–strain curves with intermediate heat treatments (HT: heat treatment at 340 °C for 20 min.)

decreases from 17 % to 10 %. An annealing of 20 min. at 340 °C is sufficient to significantly annihilate the deformation structure and recover the mechanical properties, as well as during the first annealing step than after up to 6 % stretching. Consecutive strain steps and intermediate anneals slightly decrease the tensile and yield strengths. There is no influence of the material batch. A representative set of true stress–strain curves of these experiments are presented in Fig. 2.

The initial material was in T3 condition i.e. it was solutionized, cold deformed and aged at room temperature. Due to the natural ageing period, very small precipitates and/or GP zones are present. During the successive annealing at 340 °C several phenomena can happen: recovery, precipitation/coarsening of the particles. The microstructure evolution during stretch forming with intermediate annealing of AA 2024 was investigated by Teyssier and Miroux [7]. They focused mainly on understanding the relationship between the evolution of the microstructure, effect of chemical composition and the changing mechanical properties during the stretch forming with intermediate heat treatments.

Electrical resistivity measurements were performed to follow precipitation. The observed sharp decrease of resistivity during the first annealing on T3 condition (initial material) indicates a decrease of the solute content accompanying the nucleation and/or growth of precipitates. Optical and scanning electron microscopy were used to measure the grain size and the size and density of precipitates. From the micrographs, no evidence of recrystallization was found as there was no nucleation or growth of new grains [7]. Recovery and precipitation kinetics were determined from the hardness measurements. X-ray diffraction analysis (XRD) was used to identify the different types of precipitates present during heat treatments.

The decrease of mechanical properties during the first annealing can be explained by the overageing, i.e. coarsening of precipitates, that follows the initial fast precipitation. During the subsequent annealing treatments, no visible precipitate evolution was observed and only coarsening is assumed to continue playing a role.

Recovery may happen during the first annealing and more surely during the following annealing steps to remove the work hardening introduced by stretch forming passes.

Work hardening model during stretching

To describe the deformation due to stretching, the microstructural based Nes work hardening model is used, in which the evolution of microstructure is defined by three internal state variables [10–12]. The Nes model is based on a statistical analysis of athermal storage and dynamic recovery of network dislocations. The Nes model directly takes into account the chemical composition such as the solute concentrations, grain size, volume fraction and size of the precipitates. Thus, the Nes model is quite capable to describe the changing material behavior during the ageing of heat treatable alloys. Extensive presentations of the work hardening model are given elsewhere [10–12], and only a brief overview of the analytical expressions constituting the core elements of the model are presented in the following.

Microstructure evolution

In order to provide a realistic description of the microstructure evolution the problems of athermal storage of dislocations and their annihilation by dynamic recovery need to be solved. In the present multi parameter microstructural description this implies that the evolution equations must be properly defined and solved. On the basis of the treatments of [10–12], these evolution equations can be written in compact form as follows

$$\frac{\mathrm{d}\rho_\mathrm{i}}{\mathrm{d}\gamma} = \frac{1}{\left(1 + f(q_\mathrm{b}^2 - 1)\right)} \frac{2}{b\, L_\mathrm{eff}} - \frac{\rho_\mathrm{i} v_\rho}{\dot{\gamma}} \tag{1}$$

$$\frac{\mathrm{d}\delta}{\mathrm{d}\gamma} = -\frac{2\delta^2 \rho_\mathrm{i}}{\kappa_0 \varphi} \frac{SL^2}{L_\mathrm{eff}} + \frac{b\, v_\delta}{\dot{\gamma}} \tag{2}$$

$$\frac{\mathrm{d}\varphi}{\mathrm{d}\gamma} = g\,(\rho_\mathrm{i}, \delta, \varphi) \tag{3}$$

Equations 1 and 2 represent the combined effect of athermal storage of dislocations (first term on the right-hand side in these equations) and their dynamic recovery (second term).

Athermal storage of the dislocations In the storage terms, L_{eff} is the effective slip length, the average radius the dislocation loops expand before being stored. It is determined by interactions between the mobile and the stored dislocations in the dislocation forest. If there are no other barriers than the dislocations stored in the Frank network this length scales with the spacing between the stored dislocations:

$$L_\rho = \frac{C}{\sqrt{\rho}} \tag{4}$$

Here C is a statistical parameter inversely proportional to the chance for a dislocation to become stored in the Frank network. Which depends on the solute content. However, in most commercial aluminum alloys, other barriers will be present like grain boundaries and precipitates. These barriers will also impede mobile dislocations and affect the athermal storage rate. The presence of grain boundaries and particles reduces the slip length and are taken into account by the following relation

$$\left[\frac{1}{L_{\text{eff}}}\right]^2 = \left[\frac{1}{L_\rho}\right]^2 + \left[\frac{1}{L_{\text{p}}}\right]^2 + \left[\frac{1}{L_{\text{D}}}\right]^2 \tag{5}$$

with

$$L_{\text{p}} = \frac{r/2\, f_{\text{r}}}{\kappa_3}, \quad L_{\text{D}} = \frac{D}{\kappa_2}$$

Here κ_2 and κ_3 are constants accounting for geometrical shapes and the measuring methods applied and are expected to be of the order of unity. L_{p} and L_{D} represent the slip length contributions due to precipitates and grain size (D) respectively. In Eq. 2, the first term represents the athermal storage in the newly formed subgrain boundaries and S is a cell/subboundary storage parameter, for more details see [11, 12].

Dynamic recovery The last terms in Eqs. 1 and 2 represent, respectively, the dynamic recovery effects on the dislocation density inside the cell ρ_{i}, and the subgrain size, δ. In other words, the dynamic recovery is incorporated by analyzing the stability of the cell interior dislocations ρ_{i} in terms of the *recovery* in *Frank network* and the subboundary structure in terms of *subgrain growth*.

In Eq. 1, the second term in principle defines the rate controlling annihilation frequency of the dislocations inside the subgrain. For aluminum alloys, the annihilation frequency can be written in the following form:

$$v_\rho = \rho_{\text{i}} b\, l_\rho \xi_\rho B_\rho \nu_{\text{D}} \exp\left(-\frac{U^*}{kT}\right) 2\sinh\left(\frac{V_\rho G b \sqrt{\rho_{\text{i}}}}{kT}\right) \tag{6}$$

where $l_\rho \approx b\, c_{\text{sc}}^{-1} \omega^{-1}$, $U^* = U_{\text{s}} + \Delta U_{\text{s}}$, and $V_\rho \propto 2\xi_\rho b^3$. Here, l_ρ is an activation length, c_{sc} is the solute concentration at the dislocation core, ω is a constant (≈ 1). U_{s} is the activation energy for diffusion of solute atoms and ΔU_{s} is the interaction energy between the solute atoms and the dislocation. For a detailed analysis of dynamic recovery of subgrain interior dislocations, see [12, 13].

The last term in Eq. 2 contains a velocity term corresponding to the growth rate for a given subgrain size. However, the subgrain growth phenomenon can occur only when the deformation takes place at elevated temperatures. Thus it can be neglected in this work, as the deformation takes place at room temperature. For details see [11, 12].

The misorientation aspect When dislocations are consumed by the sharpening of old boundaries they are stored in a way that does not contribute to the hardening of the material. To handle this aspect in the Nes model, the following empirical equation based on physical observations is used:

$$\frac{\mathrm{d}\varphi}{\mathrm{d}\gamma} = \left[f_{\text{II}} \frac{b\, K_{\text{II}}}{\varphi\, L_{\text{eff}}} + (1 - f_{\text{II}})\, 0.02\right]\left[1 - \left(\frac{\varphi}{\varphi_{\text{IV}}}\right)^3\right] \tag{7}$$

Here f_{II} must be equal to unity during small strain regime and vanish at larger strains. For more details, see [11, 12].

The flow stress

The flow stress, τ, at a known microstructure is commonly defined in terms of a thermal component, τ_{t}, and an athermal stress component τ_{a}, so that $\tau = \tau_{\text{t}} + \tau_{\text{a}}$. The thermal component τ_{t} is due to the rate and temperature *dependent* interactions with short range obstacles and the athermal component characterizes the rate and temperature *independent* interactions due to long range barriers.

The thermal stress To calculate the thermal stress τ_{t}, it is assumed that the mobile dislocation density ρ_{m} is proportional to the total stored dislocation density ρ, i.e. $\rho_{\text{m}} \propto m\rho$. From the Orowan equation:

$$\dot{\gamma} = \rho_{\text{m}} b\, v \tag{8}$$

The average speed of the mobile dislocations, v, may generally be expressed as:

$$v = l_a B_t \nu_D \exp\left(-\frac{U_t}{kT}\right) 2\sinh\left(\frac{V_t \tau_t}{kT}\right) \tag{9}$$

where k is the Boltzmann constant, ν_D is the Debye frequency, V_t is an activation volume and U_t is an activation energy, B_t is a constant and T is the temperature. If the solute content is sufficiently large the average dislocation speed is controlled by the dragging of elements in solid solution. Then the relaxation distance, $l_a = b\, c_{sc}^{e_t - 1}/\omega_t$, is the distance traveled by a climbing jog in between thermal activation and subsequent pinning of a solute atom. For alloys, U_t is defined as summation of activation energy for solute diffusion U_s and interaction energy between solute and dislocations ΔU_s. The activation volume is given by the spacing of solute atoms along the dislocation core, $V_t = b^2 l_s = b^3 \omega_t c_{sc}^{-e_t}$. Where l_s scales with the spacing of the solute atoms along the dislocation core, ω_t is a parameter which needs to be determined from experimental flow curves and the exponent e_t is expected to have a size in the range 0.5 to 1.

The athermal stress The athermal component, τ_a is the stress contribution due to precipitate particles (τ_p) and stored dislocations (τ_d) and are considered as long range contributions.

$$\tau_a = \tau_p + \tau_d \tag{10}$$

In age hardening aluminum alloys, the strengthening effect mainly comes from precipitation hardening due to shearing and/or bypassing of particles by dislocations. Shearing is possible only if the interface between particle and matrix is coherent i.e. continuity of the crystal structure but not necessarily the same interatomic distances. Bypass or Orowan mechanism occurs if the interface between particle and matrix is incoherent [14]. Precipitates can also indirectly contribute to the strengthening of alloys by influencing the storage of dislocations during microstructure evolution.

In this work, the contribution due to precipitates for the strengthening is described according to [15]. For this calculation the particles are assumed to be spherical and of equal size (i.e. monodispersive), equal to the mean size. This means that the constituent equations were derived on the basis of the classical analytical solutions for the dislocation-particle interaction. According to Myhr et al. [15] the stress contribution due to a population of precipitates with a radius r and volume fraction f_r is given by:

$$\tau_p = 2\beta G \frac{b}{r}\left(\frac{3 f_r}{2\pi}\right)^{1/2} \min\left[\left(\frac{r}{r_c}\right)^{3/2}, 1\right] \tag{11}$$

r_c is the critical radius deciding between shearing and bypassing mechanisms. In the above equations, G is the shear modulus of the aluminum matrix and β is a constant close to 0.5 . The precipitate size and volume fractions (input parameters) are determined by fitting the proportional limit calculated with the model of Myhr et al. [15] to experimental measurements for the different stretching and consecutive heat treatments presented in Fig. 2.

The unified relation for the stress contribution (τ_d), due to *stored dislocations* with statistical distribution of subgrain sizes in different stages of work hardening is given by:

$$\begin{aligned}\tau_d = {} & \alpha_1 G b\left[\Gamma_1\left(\frac{q_c}{\delta\sqrt{\rho_i}}\right)\sqrt{\rho_i} + \Gamma_2\left(\frac{q_c}{\delta\sqrt{\rho_i}}\right)\frac{q_c}{\delta}\right] \\ & + \hat{\alpha}_2 G b\left[\Gamma_2(0)\frac{1}{\delta} + \frac{1}{D}\right]\end{aligned} \tag{12}$$

with

$$\hat{\alpha}_2 = f_{sc}\alpha_2^{sc} + (1 - f_{sc})\alpha_2 \tag{13}$$

where

$$\alpha_2^{sc} = \alpha_1 f(q_b - 1) q_c \tag{14}$$

and

$$f_{sc} = \frac{1 - \Gamma_1\left[\frac{q_c}{\delta\sqrt{\rho_i}}\right]}{1 - \Gamma_1(1)} \tag{15}$$

Here the functions Γ_1 and Γ_2 are given as follows

$$\Gamma_1(x) = \frac{\int_0^x x^3 \mathrm{f}(x)\mathrm{d}x}{\int_0^\infty x^3 \mathrm{f}(x)\mathrm{d}x} = 1 - \exp(-5x)\sum_{n=0}^{7}\frac{(5x)^n}{n!} \tag{16}$$

and

$$\Gamma_2(x) = \frac{\int_x^\infty x^2 \mathrm{f}(x)\mathrm{d}x}{\int_0^\infty x^3 \mathrm{f}(x)\mathrm{d}x} = \frac{5}{7}\exp(-5x)\sum_{n=0}^{6}\frac{(5x)^n}{n!} \tag{17}$$

with the subgrain size distribution given by $\mathrm{f}(x) = \frac{5^5 x^4}{24}\exp(-5x)$ and $x = \left(\frac{q_c}{\delta\sqrt{\rho_i}}\right)$.

In the model, it was assumed that the initial material in T3 condition is fully recovered after the first heat treatment at 340 °C for 20 min. and the corresponding dislocation density ρ_0 was chosen to be $10^{11}\ \mathrm{m}^{-2}$. Solute concentrations come from the mass balance.

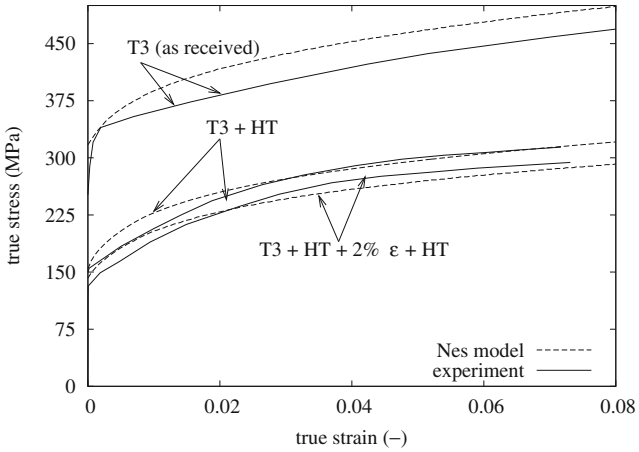

Fig. 3 True stress–strain curves with intermediate heat treatments—experiments and model (HT: heat treatment at 340 °C for 20 min.)

The sensitivity study of the Nes model in respect to the model parameters shows that only two parameters have a significant influence on the stress–strain relation:

- q_c controls the work hardening (storage of dislocation and subgrain formation and misorientation)
- ξ_ρ controls the dynamic recovery.

Both parameters have roughly similar effect on the stress–strain curve so an infinite number of combinations of these parameters can fit the experimental stress-strain curves. However, each combination gives a different result for the dislocation density and subgrain evolution. The q_c and ξ_ρ parameters are obtained by fitting the stress–strain curves on the material after first heat treatment on initial material in T3 condition at 340 °C for 20 min. giving the most realistic dislocation density and subgrain size. The fit of the strain–stress curve is not perfect for all strains, which is clearly visible in Fig. 3. All the other parameters have negligible influence on work hardening when they are varied within their range of possible values. Default values are used based on literature and the selected and fitted parameters of the Nes model are presented in Table 1. With these parameters, prediction of the stress–strain curves for the other conditions are reasonably good (Fig. 3).

Table 1 Parameters of the Nes model for AA 2024 (T3 + HT)

ν_D	$1.0 \cdot 10^{13}\,\mathrm{s}^{-1}$	b	$2.86 \cdot 10^{-10}\,\mathrm{m}$
κ	$1.3 \cdot 10^{-23}\,\mathrm{J/K}$	q_c	18.0
C	40.0	f	0.1
α_1	0.3	α_2	3.0
κ_0	$3.5\,\mathrm{m}^{-1}$	U_s	$1.5 \cdot 10^5\,\mathrm{J/mol}$
U_sd	$1.3 \cdot 10^5\,\mathrm{J/mol}$	U_t	$1.5 \cdot 10^5\,\mathrm{J/mol}$
κ_2	2.0	κ_3	0.7
φ_c	0.3489	B_t	57.0
ω_t	20.0	e_t	0.54
B_ρ	0.23	ξ_ρ	45.0
ω_s	1.0	e_ρ	0.67
B_δ	100.0	ξ_δ	20.0
e_δ	0.65	ρ_0	$1.0 \cdot 10^{11}\,\mathrm{m}^{-1}$
S_IV	0.15	q_IV	2.0
φ_IV	0.052 rad	m	0.8
r	$13.4 \cdot 10^{-9}\,\mathrm{m}$	f_r	0.013
β	0.36	r_c	$5.0 \cdot 10^{-9}\,\mathrm{m}$
c	0.0042		

Material model during heat treatment

To describe the particle coarsening and static recovery during intermediate heat treatments, simple equations based on physical observations are used.

Isothermal ageing model

During age hardening, Guinier Preston (GP) zones nucleate and grow from the quenched solid solution and deplete it. During the *nucleation* and *growth* phase, both the radius of the precipitates and their volume fraction are variable. When the solubility limit is reached, precipitates coarsen by competitive *growth* and in the model the radius of the precipitates is considered as a variable and the volume fraction of the precipitates becomes constant. It was found in the experiments of Teyssier and Miroux [7] that nucleation and growth of GP zones is observed mainly during the first 2 min. of initial heat treatment at 340 °C for 20 min. on T3 condition and no or very little nucleation of GP zones were observed in the consecutive heat treatments. Hence, ageing is controlled by the coarsening kinetics and the particle coarsening effects are considered by a relatively simple semi-empirical expression. Coarsening is described here by the growth of the mean particle radius r of assumed spherical shape with time t. No attempt has been made at present to include changes in particle shape or in the distribution of particle size during coarsening, though it is acknowledged that these can be important effects. According to Rylands et al. [16], the size evolution in each annealing sequence is:

$$r = \left(r_i^n + kt\right)^{1/n} \tag{18}$$

with

$$k = \frac{k_0}{T} \exp\left(-\frac{Q}{RT}\right) \tag{19}$$

Table 2 Volume fraction and size of the particles calculated for different stretching and consecutive heat treatments

Condition	Vol. frac (%)	Size (m)
T3	1.3	$5.0 \cdot 10^{-9}$
T3+HT	1.3	$13.4 \cdot 10^{-9}$
T3+HT+2 to 6% stretch+HT	1.3	$16.6 \cdot 10^{-9}$

where Q is the activation energy for volume diffusion of Cu atoms between particles which is equal to 136 kJ/mol, R is the universal gas constant, t is the process annealing time and the bulk diffusion coefficient $n = 3$ is considered in the simulations. k_0 is then obtained by fitting the predicted particle radius presented in Table 2 and equal to $4.5 \cdot 10^{-13}\mathrm{K{\cdot}m^3/s}$.

Static recovery model

The term "recovery" refers to the restoration of material properties back to their original or undeformed state after deformation and prior to recrystallization [17]. Static recovery is specifically attributed to the process that occurs after deformation whereas dynamic recovery takes place during the course of deformation. It is well known that recovery of most metals is primarily due to changes in the dislocation structure [18]. Dislocation recovery is not a simple microstructural change, but is constituted by a series of events: dislocation tangling immediately after deformation, dislocation cell formation, annihilation of dislocations within cells, subgrain formation and subgrain growth [13, 18].

In this work, an empirical approach based on physical observations of recovery kinetics based on Humphreys type 2 model [18] is used. According to Humphreys, the total dislocation density evolution due to recovery kinetics is given by:

$$\rho = \left[\sqrt{\rho_0} + \left(\sqrt{\rho_\mathrm{d}} - \sqrt{\rho_0}\right)\left(1 + (q-1)Bt\right)^{\left(-\frac{1}{q-1}\right)}\right]^2 \quad (20)$$

where ρ_0 is the total dislocation density of fully soft material, ρ_d is the dislocation density of deformed configuration just before annealing and t is the annealing time. The recovery kinetics parameters B and q are material and temperature dependent and fitted for the temperature of interest. Usually the exponent q is found to be in the range of 3 to 5; and $q = 4$ is chosen in this work.

When deforming the material after annealing, it is expected that the deformation of the recovered structure starts with stage II. Therefore the in-cell dislocation density during recovery is related to the total dislocation density using the same scaling relation as during stage II:

$$\rho_\mathrm{i} = \frac{\rho}{f\left(q_\mathrm{b}^2 - 1\right) + 1} \quad (21)$$

The fully soft dislocation density is taken as $\rho_0 = 10^{11}\mathrm{m}^{-2}$ According to the experimental results, 20 min. annealing at 340 °C is supposed to be enough to obtain a fully recovered microstructure. The parameter B is then chosen in such a way that ρ_i gets close to ρ_0 after 20 min. annealing at 340 °C. It is found that after a sharp decrease, ρ_i decreases only slowly with time, whatever the value of B. A value of $B = 0.1\mathrm{s}^{-1}$ is chosen as a compromise between the value of ρ_i after 20 min. annealing at 340 °C and the rate of decrease of ρ_i at the beginning of annealing.

The yield criterion

To describe the anisotropy and biaxial behavior of the sheet, the Vegter yield function [20] is used. The Vegter yield function is one of the most accurate yield functions for aluminum alloy sheets defined in plane stress condition. The Vegter yield locus is constructed in principal stress space and uses Bezier interpolation to connect the measured yield stresses in equi-biaxial, plane strain tension, uniaxial tensile and pure shear tests as shown in Fig. 4. This leads to 4 stress points in the region where $\sigma_1 > \sigma_2$. For the situations where $\sigma_1 < \sigma_2$ can be determined if the sample is rotated by 90 °. The compressive part of the yield locus is usually not measured from the experiments, but is defined by assuming that the initial yield stress in compression is equal to that in tension.

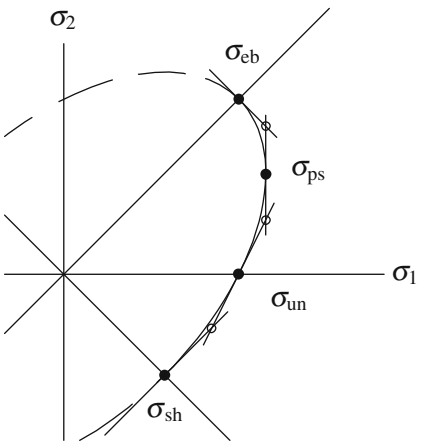

Fig. 4 Basic stress points required to construct the Vegter yield locus

Table 3 Measured stress and strain ratios for the AA 2024-O sheet (Vegter yield locus data)

Angle with RD	0°	45°	90°
$(\sigma_1/\sigma_1^{RD})_{un}$	1.0	0.98	0.99
f_{ps}	1.14	1.1	1.09
f_{sh}	0.576	0.579	0.577
f_{bi}	0.96		
R-value	0.52	0.67	0.52
$(\varepsilon_2/\varepsilon_1)_{bi}$	1.0635		

Anisotropy of the sheet is captured by using the flow stresses of the experiments under different angles with respect to the rolling direction. The flow stresses on intermediate angles are defined by a harmonic interpolation function.

In the implementation of this model for an orthogonal material, experiments in 3 directions (0°, 45° and 90°) are required to determine the 14 material parameters. The parameters for the investigated AA 2024 alloy are given in Table 3.

Stretch forming of aircraft skin experiments

A number of sheets have been stretched using manually determined trajectory of the grippers. The dimensions of the sheet are 1130 ×1920 ×3.5 mm. Five intermediate heat treatments are used. To measure the strain in the final part a grid of dots with known dimensions was applied to the undeformed sheet. Due to the large dimensions of the sheet only part of the sheet which is known to deform most was measured. The final part is shown in Fig. 5.

The PHAST^{TM} strain measurement system [21] has been used to measure the strains after stretch forming. This system is based on 3D image processing. Digital photos are taken from different positions of the product

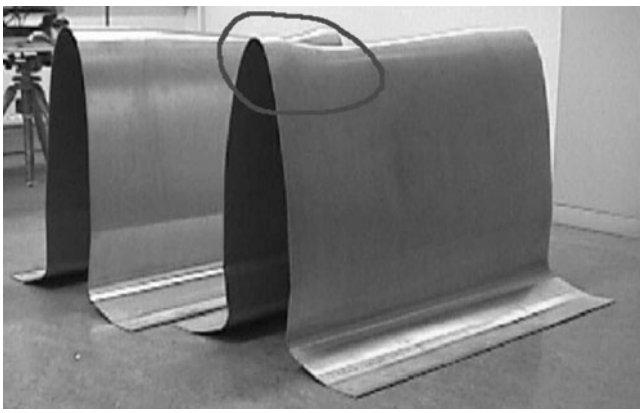

Fig. 5 Skin parts after stretch forming

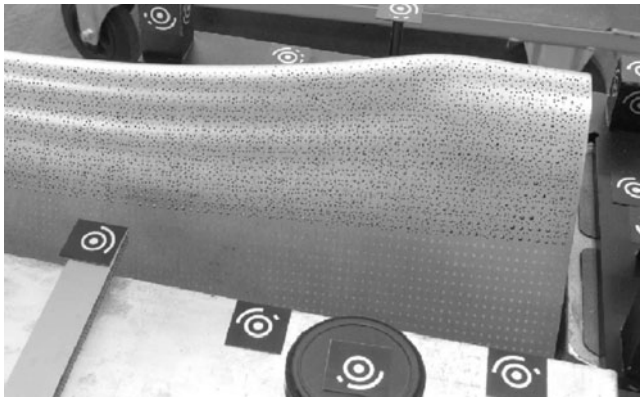

Fig. 6 Parts with recognized grid points and beacons

and some beacons. The strains are calculated from the recognized grid points and beacons (Fig. 6) using photogrammetry.

A correction in the thickness calculation must be considered as it was calculated from the strains measured on the outer plane of the sheet instead of the midplane. In this case the thickness is corrected up to 0.1 mm, as was confirmed by direct thickness measurements at the edges.

Finite element simulations

The initial shape of the sheet and tools is shown in Fig. 7. As the geometry of the die is symmetric and therefore the geometry of the final product is also symmetric only half of the sheet is modeled. The part of the sheet that is clamped between the gripper jaws is not modeled, as ideal clamping is assumed. The prescribed displacement boundary conditions are applied to the

Fig. 7 Initial Sinusoidal shape of sheet and tools

remaining edges of the sheet in the gripper jaws. The cheeks (part of the grippers which are making contact with the product) are modeled as cylinders. Both cheek nodes and prescribed sheet nodes are given the same prescribed displacements.

It can be seen in Fig. 7 that the initial shape of the sheet is curved, which agrees with the industrial practice as the sheet is slightly bent before clamping it into the machine. The initial curvature is modeled by taking the initial shape of the sheet equal to a shallow cosine. This shape is equal to the shape of the buckle mode of a compressed sheet. In this example the edges of the sheet are moved only 15 mm inwards. It is assumed that this bend causes no stresses and plastic deformations in the sheet. By modeling this initial cosine shape it is ensured that the sheet deforms in the correct upward direction, when the sheet is draped around the die in the first part of the stretch process. This also avoids numerical instabilities during the finite element simulation.

The cheeks and die are assumed to be rigid bodies, i.e. they are undeformable with respect to the sheet. A penalty method is used to describe the contact between the rigid tools and the sheet. The friction between the sheet and rigid tools (die and cheeks) is described with Coulomb's friction model with a friction coefficient of 0.1 .

The sheet has been meshed with 2810 triangular elements with a refinement close to the symmetry line. The size of the element edges ranges from 20 to 40 mm. The used discrete Kirchhoff shell elements [19], take membrane as well as bending stiffness into account.

The used trajectory of the grippers is shown in Fig. 8. It is a piecewise linear approximation of the trajectory used for the experiments. The rotations of the grippers have been neglected, as they are relatively small. The positions at which an intermediate heat treatment is given to the sheet are marked.

Two different hardening models: a phenomenological power law model and the physically based Nes model are used for the simulations. The power law parameters are determined from the experimental stress–strain curves presented in Fig. 2.

In the complete stretch forming process on a saddle shaped skin part, the sheet was annealed five times. In the simulation the annealing step is included by using the simple models for particle coarsening and static recovery presented in the previous section. During the heat treatment, the new values for the precipitate size and total dislocation density for a given annealing temperature and time are calculated. Further deformation steps are continued using the physically based Nes work hardening model with the calculated values of precipitate size and dislocation density at every integration

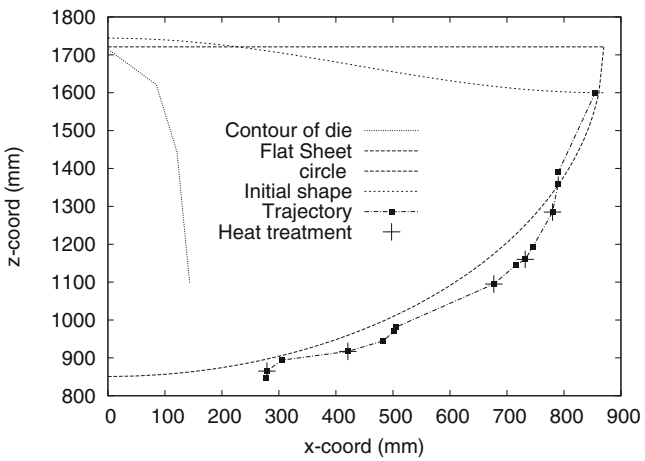

Fig. 8 Trajectory of the grippers used in the simulation

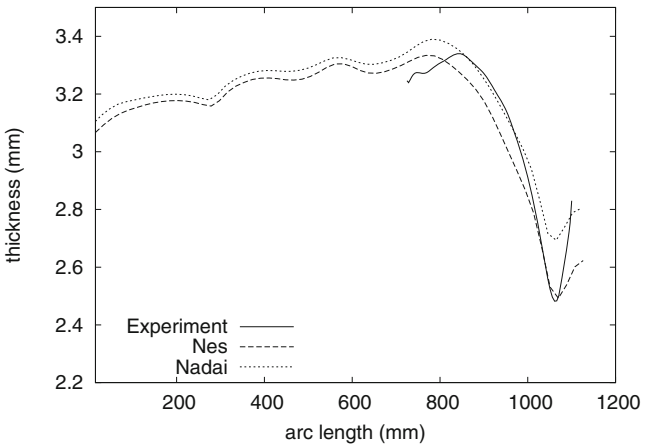

(a) with heat treatment

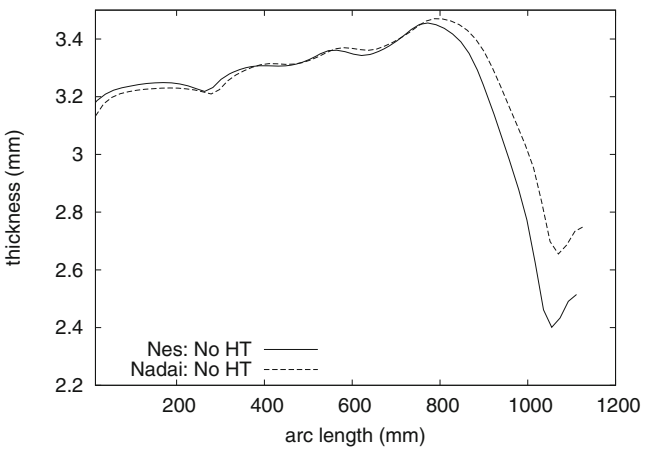

(b) without heat treatment

Fig. 9 Thickness along symmetry line with and without heat treatments (HT)

point of the DKT elements. In the case of the power law model, the annealing step is included only phenomenologically by resetting the (equivalent) plastic strain to zero, thus deleting complete work hardening in all integration points.

In Fig. 9 the thickness along the symmetry line is presented after all stretching phases with and without heat treatments for the Nes and Nadai models. With heat treatments, the deformations are stable and they are almost completely kinematically determined. The physically based Nes model gives better thickness prediction, particularly at the critical region of the part as shown in Fig. 10, than the phenomenological Nadai model (see Fig. 9a). The die force–gripper displacement diagram in Fig. 11a shows a large drop in the die force because the stresses are set to zero after the heat treatment. For the Nes model, the force does not completely drop to zero because the work hardening effect is not completely deleted and residual stresses are left in the material.

Figure 11b shows that without intermediate heat treatments steps, the die force is higher as there is no removal of work hardening. Correspondingly without heat treatments, more thinning is observed in the critical region of the part shown in Fig. 9b. This thinning is more severe with the Nes model. Apart from the heat treatments, a drop in vertical force on the die, for example for the gripper displacement between 500 mm

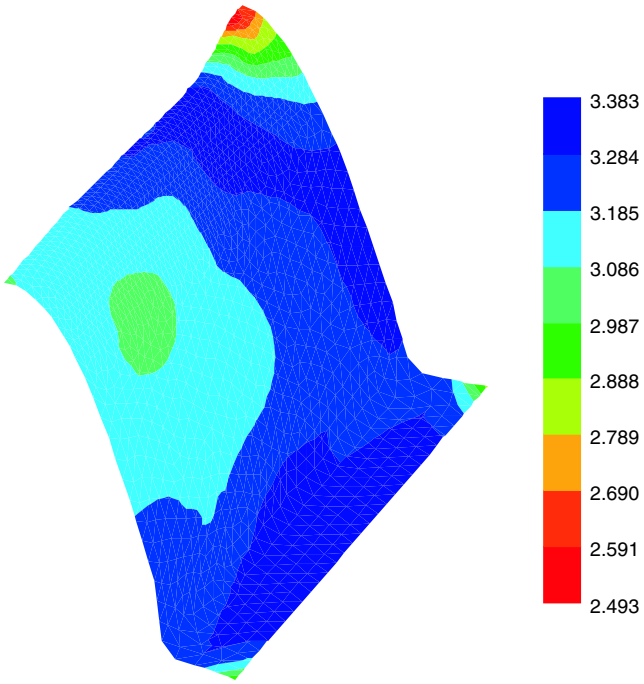

Fig. 10 The predicted thickness in the final product with heat treatments using Nes model

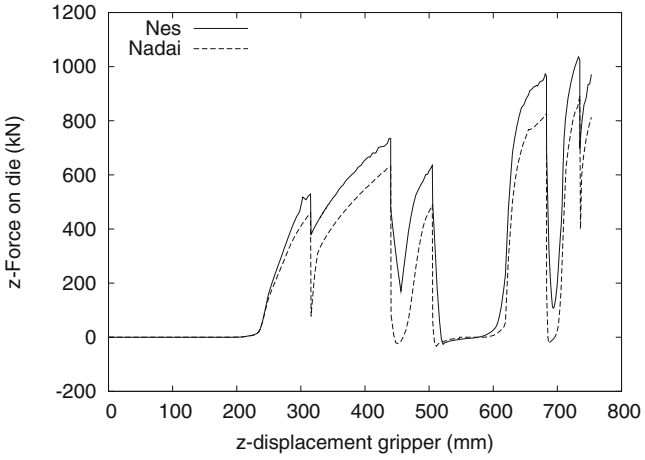

(a) with heat treatment

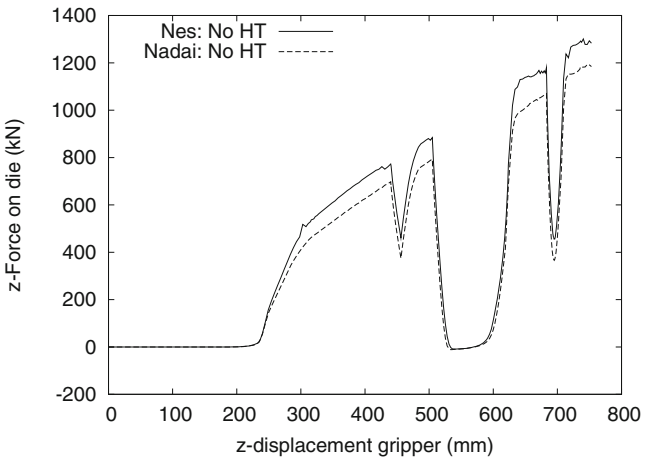

(b) without heat treatment

Fig. 11 Vertical force on die with and without heat treatments (HT)

to 600 mm corresponds to loss of contact between the die and the sheet.

In Fig. 12, the effect of different approaches for heat treatments are studied. In this study, simulations are performed with a physics based approach for heat treatments by considering the particle coarsening and static recovery and a phenomenological approach i.e. assuming the work hardening effect is completely removed by resetting plastic strains to zero. Simulations are also performed without intermediate heat treatments. In all the three situations, the work hardening effect is described using the physically based Nes model. From Fig. 12a, it is clearly seen that the force–displacement curve is more stable with the physically based approach for heat treatments than the phenomenological approach as it shows jiggles in the force–displacement curve. With the phenomenological approach, after every intermediate heat treatment the vertical force on the die

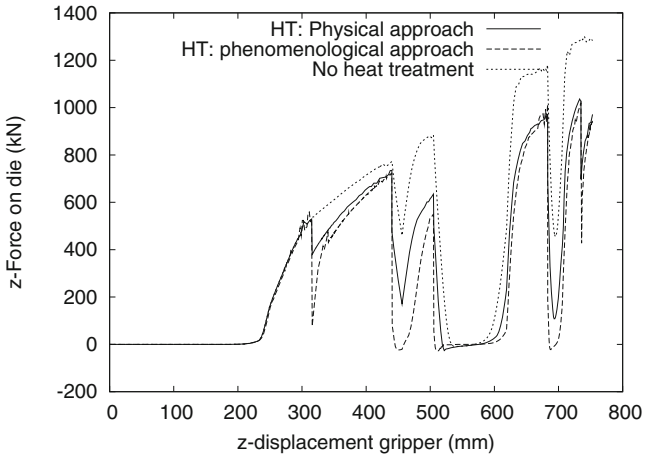

(a) Vertical force on die

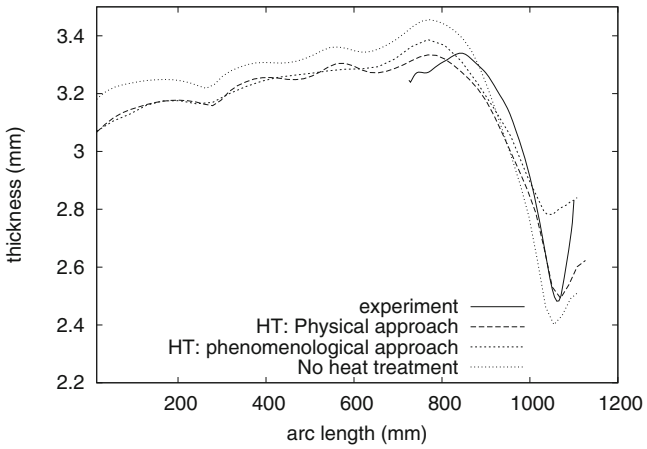

(b) Thickness along symmetry line

Fig. 12 Influence of heat treatment on predicted vertical force on die and thickness along symmetry line

almost drops to zero as the stresses are completely removed. However, this is not completely realistic. From the thickness along the symmetry line plot shown in Fig. 12b it follows that with the phenomenological approach the thinning effect in the critical region is underestimated and the physically based approach is much better. Without heat treatments too much thinning effect is observed.

Conclusions

The main objective of this work was to develop and use a suitable numerical model for the finite element analysis of the stretch forming of aircraft skin parts with intermediate heat treatments. An important part of the numerical model is the modeling of the material behavior. Both the hardening behavior during the stretching process, and the reduction of work hardening behavior during the heat treatment process are considered. Two hardening models are compared: a phenomenological Nadai hardening model and a physically based model according to Nes. The reduction in work hardening during heat treatment is modeled by considering the underlying physics such as the overageing model for particle coarsening and the static recovery model. A phenomenological approach is also used for comparison by deleting all work hardening effect from the previous stretching phases.

From the presented simulations, it can be concluded that the physics based material modeling gives better results. The predicted thickness distribution especially in the critical region of the part using the Nes model for work hardening and the overageing and static recovery models for intermediate annealing gives better agreement with the experiments.

In this work the material models are compared only with uniaxial tensile experiments and the predicted thickness distribution are used for the validation. In order to have more confidence on the implemented material models, further validation of FEM results such as the vertical force on die and the strain distribution would be useful. There is also room for improvement in the material modeling as in the current models, the effect of particle coarsening and static recovery are treated separately. In reality, the effect of particle coarsening and recovery on the reduction of work hardening during heat treatments is coupled.

Acknowledgements This research was carried out under the project number MC1.02106 in the framework of the Research Program of Materials innovation institute M2i (http://www.m2i.nl), the former Netherlands Institute for Metals Research.

References

1. McMurray RJ, O'Donnell M, Leacock AG, Brown D (2009) Modelling the effect of pre-strain and inter-stage annealing on the stretch forming of a 2024 aluminum alloy. Key Eng Mater 410:421–428
2. Straatsma EN, Velterop L (2004) Influence of heat treatments and straining steps on mechanical properties in the stretch forming process. In: Muddle BC, Morton AJ, Nie JF (eds) 9th International conference on aluminum alloys, Brisbane, Australia, pp 771–776
3. Hol J (2009) Optimization of the stretch forming process using the finite element method. Master Thesis, University of Twente

4. O'Donnell M, Banabic D, Leacock AG, Brown D, McMurray RJ (2008) The effect of pre-strain and inter-stage annealing on the formability of a 2024 aluminum alloy. Int J Mater Form 1:253–256
5. Jaspart O, François A, Magotte O, D'Alvise L (2004) Numerical simulation of the stretch forming process for prediction of fracture and surface defect. In: 7th ESAFORM conference on material forming, Trondheim, Norway, pp 499–502
6. Wisselink HH, van den Boogaard AH (2005) Finite element simulation of the stretch-forming of aircraft skins. In: Smith LM, Pourboghrat F, Yoon JW, Stoughton TB (eds) Proceedings Of The 6th international conference and workshop on numerical simulation of 3D sheet metal forming processes, Detroit, USA, pp 60–65
7. Teyssier E, Miroux A (2004) Microstructure evolutions during industrial sheet forming of AA 2024 aluminum alloy. Internal report: P04.4.063, Netherlands Institute for Metals Research (NIMR)
8. Bray JW (1990) Properties and selection: Nonferrous alloys and special purpose materials. In: Davis JR, Allen P, Lampman SR, Zorc TB (eds) Metals Handbook, ASM International, vol 2. Materials Park, Ohio, pp 29–72
9. Velterop L (2004) Stretch forming of aluminum—Mechanical properties AA 2024 Alclad. Internal report: NLR-TR-2004-148, National Aerospace Laboratory NLR
10. Nes E (1998) Modelling of work hardening and stress saturation in FCC metals. Prog Mater Sci 145:129–193
11. Marthinsen K, Nes E (2001) Modelling strain hardening and steady state deformation of Al–Mg alloys. Mater Sci Technol 17:376–388
12. Nes E, Marthinsen K (2002) Modelling the evolution in microstructure and properties during plastic deformation of FCC-metals and alloys—an approach towards a unified model. Mater Sci Eng A, 322:176–193
13. Nes E (1994) Recovery revisited. Acta Metall Mater 43:2189–2207
14. Reppich B (1993) A comprehensive treatment. In: Cahn RW, Hassen P, Kramer EJ (eds) Materials science and technology, vol 6. VCH, Weinheim, Germany, p 93
15. Myhr OR, Grong O, Andersen SJ (2001) Modelling of the age hardening behavior of Al–Mg–Si alloys. Acta Mater 49:65–75
16. Rylands LM, Wilkes DMJ, Rainforth WM, Jones H (1994) Coarsening of precipitates and dispersoids in aluminum alloy matrices: a consolidation of the available experimental data. J Mater Sci 29:1895–1900
17. Kuo CM, Lin CS (2007) Static recovery activation energy of pure copper at room temperature. Scripta Mater 57:667–670
18. Humphreys FJ, Haterly M (2004) Recrystallization and related annealing phenomena. Elsevier Ltd, Oxford, UK
19. Batoz JL, Bathe KJ, Ho LW (1980) A study of three-node triangular plate bending elements. Int J Numer Methods Eng 15:1771–1812
20. Vegter H, van den Boogaard AH (2006) A plane stress yield function for anisotropic material by interpolation of biaxial stress states. Int J Plast 22:557–580
21. Atzema EH (2003) The new trend in strain measurements: fast, accurate and portable: PHAST^{TM}. In: Singh UP, et al (eds) Sheet metal 2003: Proc. of 10th Int. Conf., pp 405–412